



















The chemical enrichment in the early Universe as probed by *JWST* via direct metallicity measurements at $z \sim 8$

Mirko Curti ^{1,2}★ Francesco D'Eugenio ^{1,2} Stefano Carniani ³ Roberto Maiolino,^{1,2,4} Lester Sandles,^{1,2} Joris Witstok ^{1,2} William M. Baker ^{1,2} Jake S. Bennett ^{1,5} Joanna M. Piotrowska ^{1,2} Sandro Tacchella ^{1,2} Stephane Charlot,⁶ Kimihiko Nakajima ⁷ Gabriel Maheson,^{1,2} Filippo Mannucci ⁸ Amirnezam Amiri,^{8,9} Santiago Arribas,¹⁰ Francesco Belfiore ⁸, Nina R. Bonaventura,¹¹ Andrew J. Bunker,¹² Jacopo Chevallard ¹², Giovanni Cresci,⁸ Emma Curtis-Lake,¹³ Connor Hayden-Pawson ^{1,2} Gareth C. Jones,¹² Nimisha Kumari ¹⁴ Isaac Laseter,¹⁵ Tobias J. Looser,^{1,2} Alessandro Marconi,^{8,9} Michael V. Maseda ¹⁵, Jan Scholtz,^{1,2} Renske Smit ¹⁶ Hannah Übler ^{1,2} and Imaan E. B. Wallace ¹²

Affiliations are listed at the end of the paper

Accepted 2022 September 22. Received 2022 September 22; in original form 2022 July 26

ABSTRACT

We analyse the chemical properties of three $z \sim 8$ galaxies behind the galaxy cluster SMACS J0723.3-7327, observed as part of the Early Release Observations programme of the *James Webb Space Telescope*. Exploiting [O III] λ 4363 auroral line detections in NIRSpec spectra, we robustly apply the direct T_e method for the very first time at such high redshift, measuring metallicities ranging from extremely metal poor ($12 + \log(\text{O}/\text{H}) \approx 7$) to about one-third solar. We also discuss the excitation properties of these sources, and compare them with local strong-line metallicity calibrations. We find that none of the considered diagnostics match simultaneously the observed relations between metallicity and strong-line ratios for the three sources, implying that a proper re-assessment of the calibrations may be needed at these redshifts. On the mass–metallicity plane, the two galaxies at $z \sim 7.6$ ($\log(M_*/M_\odot) = 8.1, 8.7$) have metallicities that are consistent with the extrapolation of the mass–metallicity relation at $z \sim 2\text{--}3$, while the least massive galaxy at $z \sim 8.5$ ($\log(M_*/M_\odot) = 7.8$) shows instead a significantly lower metallicity. The three galaxies show different level of offset relative to the Fundamental Metallicity Relation, with two of them (at $z \sim 7.6$) being marginally consistent, while the $z \sim 8.5$ source deviating significantly, being probably far from the smooth equilibrium between gas flows, star formation, and metal enrichment in place at later epochs.

Key words: galaxies: abundances – galaxies: evolution – galaxies: general – galaxies: ISM.

1 INTRODUCTION

The study of the abundances of heavy elements (the ‘metallicity’) in the interstellar medium (ISM) of galaxies provides precious insights on the physical processes responsible for their formation, and on how the relative importance of such processes has changed across cosmic time (e.g. Ma et al. 2016; Davé et al. 2017; Torrey et al. 2019; Langan, Ceverino & Finlator 2020, see also the review by Maiolino & Mannucci 2019).

In the local Universe, the metallicity of the gas-phase is observed to correlate tightly with some of the primary galactic properties. Specifically, the metallicity depends on the stellar mass of the galaxy (mass–metallicity relation, MZR; Tremonti et al. 2004) and has a secondary (inverse) dependence on the star formation rate (SFR; Ellison et al. 2008). This metallicity- M_* -SFR relation has been called the Fundamental Metallicity Relation (FMR; Mannucci et al.

2010; Mannucci, Salvaterra & Campisi 2011; Curti et al. 2020a), a signature of the smooth, long-lasting equilibrium between gas flows and secular evolution (e.g. Bouché et al. 2010; Lilly et al. 2013).

In the past fifteen years, major efforts have been dedicated to explore the metallicity of high-redshift galaxies through massive spectroscopic surveys in the near-IR (e.g. Maiolino et al. 2008; Mannucci et al. 2009; Zahid, Kewley & Bresolin 2011; Steidel et al. 2014; Zahid et al. 2014; Erb et al. 2016; Strom et al. 2017; Curti et al. 2020b; Sanders et al. 2021, among many others). These works have established that the mass–metallicity relation is already in place up to $z \sim 3.3$, and that it evolves with redshift, in the sense that higher redshift galaxies appear metal deficient compared to galaxies of similar stellar mass at later epochs. However, when taking into account the secondary dependence of the MZR on the SFR, as described by the FMR framework, any evolution is apparently canceled out at least up to $z \sim 3.3$ (e.g. Mannucci et al. 2010; Cresci, Mannucci & Curti 2019; Sanders et al. 2021). This finding implies that galaxies up to $z \sim 3.3$ follow, on average, the same smooth evolution as local galaxies, and that the evolution of the MZR is

* E-mail: mc2041@cam.ac.uk

a consequence of $z \sim 2\text{--}3$ galaxies having higher SFR (living at the epoch of the peak of the cosmic star formation rate density; Madau & Dickinson 2014), therefore populating preferentially the low-metallicity region of the same, non-evolving FMR. Together with the existence of the main sequence of star formation (e.g. Noeske et al. 2007; Popesso et al. 2022; Sandles et al. 2022; and references therein) this is an indication that secular rather than stochastic processes dominate the evolution of galaxies at these epochs.

Pushing the exploration of galaxy metallicities to redshifts higher than ~ 3.3 has proven very challenging so far due to the intrinsic technical limitations of current astronomical facilities, as the primary (optical) nebular diagnostics required to measure the gas-phase metallicity from galaxy spectra are redshifted outside the wavebands observable from the ground (but see Troncoso et al. 2014; Shapley et al. 2017; Witstok et al. 2021).

An additional problem is that metallicity determinations generally rely on adopting locally calibrated strong-line diagnostics, as temperature-sensitive auroral lines are usually too faint to be detected, preventing the use of the more robust and ‘direct’ electron-temperature (T_e) method. However, it is not clear whether the strong-line calibrations derived in the local universe are valid for distant galaxies, which have drastically different properties (Maiolino & Mannucci 2019). To date, auroral lines have been observed only in a small number of intermediate-redshift ($z \sim 1\text{--}3$) galaxies, and constitute mostly serendipitous, low-significance detections (e.g. Christensen et al. 2012; Patrício et al. 2018; Sanders et al. 2020).

This observational landscape is set to be revolutionized by the advent of the *James Webb Space Telescope* (*JWST*) and its near-IR spectrograph NIRSpec (Ferruit et al. 2022; Jakobsen et al. 2022), which has opened the capability of obtaining multi-object spectroscopic observations in the near-IR from space (up to $5.3\ \mu\text{m}$), combining high multiplexing with a sensitivity much higher than any current and past facility.

The first *JWST*/NIRSpec spectra have been recently released within the context of the Early Release Observations, and were obtained by targeting galaxies lensed by the cluster SMACS J0723.3-7327 (Ebeling, Edge & Henry 2001; Ebeling et al. 2007, 2010; Mann & Ebeling 2012; Ebeling et al. 2013; Repp, Ebeling & Richard 2016; Repp & Ebeling 2018), providing clear detections of nebular lines in galaxies out to $z = 8.5$, which can be used to characterize the chemical enrichment of the ISM at the Epoch of Reionization (EoR), and beyond. Most remarkably, some of these spectra present clear detections of the $[\text{O III}]\lambda 4363$ auroral line, which can be used to robustly measure the gas metallicity with the T_e method for the very first time at such high redshifts.

In this paper, we extract the direct metallicity of such galaxies at $z \sim 8$, which have individual detections of auroral lines, and test whether they follow the same strong-line metallicity calibration as local galaxies. In addition, we investigate whether these galaxies, probing the EoR, follow the same metallicity scaling relations as lower redshift galaxies or exhibit evidence for evolution.

This paper is organized as follows. In Section 2 we describe observations, data processing, and data analysis. In particular, we discuss the different steps we have implemented to properly process and calibrate the data by using publicly available information. We also describe our emission lines fitting procedure, and how SED fitting was performed on NIRCAM photometry to derive different physical properties of these galaxies. In Section 3, we discuss the emission-line properties of our targets, in terms of Balmer decrements and dust attenuation, excitation-diagnostic diagrams, and metallicity properties as derived with the T_e method. We also

compare the observed line ratios and metallicity with some of the most widely adopted strong-line abundance diagnostics calibrated on local galaxies. In Section 4, we discuss the observed metallicity properties of these targets in the framework of the most relevant metallicity scaling relations, i.e. the mass–metallicity and the fundamental metallicity relation. Finally, in Section 5 we report our conclusions.

Throughout this work, we assume a standard lambda cold dark matter cosmology with $H_0 = 70\ \text{km s}^{-1}$, $\Omega_m = 0.3$, and $\Omega_\Lambda = 0.7$.

2 OBSERVATIONS, DATA PROCESSING, AND DATA ANALYSIS

2.1 NIRSpec spectroscopy

2.1.1 NIRSpec observations

We use publicly available data from the Early Release Observations of the cluster SMACS J0723.3-7327 (Program ID: 2736, Pontoppidan et al. 2022). The NIRSpec observations consist of two pointings with the same Multi Shutter Array (MSA) configuration but different acquisition stars (and different filters for the acquisition); in the following, we refer to these two observations as Obs 7 and Obs 8.

NIRSpec observations were carried out by using the disperser-filter combinations G235M/F170LP and G395M/F290LP, which cover the wavelength range between 1.66 and $5.16\ \mu\text{m}$ and provide spectra with a spectral resolution of $R \sim 1000$. For each observation, three nodding positions of 20 groups and two integrations each were performed for each grating setup. The total exposure time of the two individual pointings is the same and corresponds to $8840\ \text{s}$ for each grating. While shutters were opened on 35 targets, in this paper we only focus on the three targets with the highest redshift: ID 4590 ($z = 8.4953$), ID 6355 ($z = 7.6643$) and ID 10612 ($z = 7.6592$). These redshifts are based on emission-line velocities measured on the *JWST* spectra (see Section 2.1.3).

2.1.2 NIRSpec data reduction

We have retrieved the level 2 data (i.e. count rate maps) from the MAST archive, but we have then reprocessed the data through the GTO pipeline (NIRSpec/GTO collaboration, in preparation). As most of the processing steps use the same algorithms that the pipeline used to generate the MAST archive products (see fig. 11 and section 4.3 of Ferruit et al. 2022), the resulting 2D spectra are not very different from those provided by the standard MAST pipeline; however, we perform our own optimized extraction aperture and bad/cosmic pixel flagging and masking. Most importantly, to mitigate the fact that many of the calibration reference files used by the pipeline may still correspond to ground data or be model based,¹ we have generated a correction to the response function by analysing the observation of the spectrophotometric calibration star 2MASS J18083474+6927286, observed during commissioning, and publicly available through programme *JWST* 1128. We note that this star has been subsequently removed from the list of primary calibrators for *JWST*, on account of its variability ($\sigma = 0.41$ per cent; Gordon et al. 2022); however, for our purposes, this adds a negligible amount of uncertainty. Specifically, the resulting spectrum of the star processed in the same way as the scientific targets was compared with its intrinsic spectrum from STScI (astronomical catalogue CALSPEC;

¹<https://jwst-docs.stsci.edu/jwst-calibration-pipeline-caveats>

Bohlin, Gordon & Tremblay 2014; Bohlin, Hubeny & Rauch 2020) to derive a more accurate flux calibration.

Given that our sources are marginally resolved, we consider both the assumption of point-like source and extended source to correct for path-losses. However, as the sources are fairly compact (especially compared to the point spread function, PSF, at long wavelengths), we use the point-source assumption for our fiducial analysis. We note that at long wavelengths (F290LP filter, with PSF comparable or larger than the shutter size), which are of greatest interest in this paper, the relative flux correction does not strongly depend on which of the two cases is adopted, while providing an offset of ~ 2 on the absolute calibration; yet, we verified that adopting the extended-source corrections does not significantly affect the main results of the paper. Background subtraction was performed through the standard technique of subtracting the average of two nodding positions from the other position.

We also inspect the exposures of the individual nods in order to identify artefacts that might have escaped automated flagging and other potential issues. We note that the auroral lines are detected in the individual exposures, hence confirming their detection at high confidence level, with the exception of galaxy ID 4590 ($z = 8.5$), for which no emission lines are detected in one of the nods of Obs 7. By inspecting the 2D images before background subtraction, it was found that, although not identified as faulty, shutter [3,27,167], on which source ID 4590 was nodded, did not open in Obs 7. As a consequence, for source ID 4590, we use Obs 8 and only the two noddings of Obs 7 for which the source is in open shutters.

Stacking was performed with the GTO pipeline, taking into account the variances and quality arrays of both observations. The resulting spectra are shown in Fig. 1. Note that these spectra are in F_λ (while the spectra provided by MAST archive are in F_ν). These spectra can be retrieved from a publicly accessible repository²

2.1.3 Spectral fitting

In our analysis, we use only data from the G395M/F290LP disperser/filter combination, because it covers the entire rest-frame wavelength range relevant to this work. We measure line fluxes using PPXF, the penalized pixel fitting algorithm of Cappellari (2017). We rebin the spectra to a regular grid in linear velocity space, using the original velocity sampling as uniform pixel size (102 km s^{-1}).³ To model the continuum, we use a library of simple stellar-population (SSP) spectra coupled with a 10th-order multiplicative Legendre polynomial. The SSP spectra are the high-resolution ($R = 10\,000$) synthetic spectra from the C3K library (Conroy et al. 2019) with MIST isochrones (Choi et al. 2016) and solar abundances. Note that repeating our fit with a polynomial background does not change our results. The emission lines and continuum are tied together to have the same velocity offset and velocity dispersion (while PPXF also takes into account the variable spectral resolution). For $[\text{O II}]\lambda\lambda 3727, 3729$, we constrain the doublet ratio to its physical range; for $[\text{Ne III}]\lambda\lambda 3870, 3969$, we fixed the ratio to 0.31. As a sanity check, for $[\text{O III}]\lambda\lambda 4959, 5007$, we leave the ratio a free parameter and check that the recovered value is consistent within the errors with the theoretical expectation of 0.34 (e.g. Osterbrock & Ferland 2006). We perform two fits: after the initial fit, we reject spectral pixels beyond four standard deviations from the best-fitting model,

²Available at <https://doi.org/10.5281/zenodo.6940561>.

³We verified that e.g. the $\text{H}\delta/\text{H}\beta$ line ratios are on average unchanged when fitting the data without rebinning.

then repeat the procedure with outliers masked to obtain the final measurements.

The resulting fitted lines are shown in Fig. 1 (with zoomed insets for lines most relevant for this work) and the resulting line fluxes relative to $\text{H}\beta$ are given in Table 1. The uncertainties are taken from PPXF (up-scaled by $\sqrt{\chi^2}$), but we find them consistent with the values obtained from running one hundred Monte Carlo realizations of the best-fitting spectrum, with random Gaussian noise taken from the noise vector.

2.2 NIRCcam imaging

2.2.1 NIRCcam observations

We use the deep NIRCcam imaging data of SMACS J0723.3-7327 from the Early Release Observations (Programme ID 2736) in the F090W, F150W, F200W, F277W, F356W, and F444W filters, which cover an observed wavelength range of $\lambda_{\text{obs}} = 0.8\text{--}5 \mu\text{m}$. We reduce the raw level-1 data products with the public JWST pipeline (v1.6.1),⁴ using the latest available calibration files (CRDS_CTX = jwst_0927.pmap). An additional background subtraction is performed on the final mosaiced images by using PHOTUTILS to mask pixels identified with sources and then measuring the background with PHOTUTILS.BACKGROUND2D.

We conduct aperture photometry on the final mosaics with a range of aperture sizes, given the extended morphology of the three galaxies in this study and their close-by neighbours. Specifically, we use circular apertures with radii from 0.2 to 0.4 arcsec. We perform an aperture correction with the help of WebbPSF (Perrin et al. 2015).⁵ We find that the final SFRs and stellar masses only weakly depend on the aperture size. For simplicity, we therefore assume a fiducial size of 0.3 arcsec. We estimated the uncertainties of these fluxes from the error maps of the mosaic images.

2.2.2 Spectral energy distribution fitting

We perform SED modelling of the NIRCcam photometry with the Bayesian code BEAGLE (Chevallard & Charlot 2016) with the main aim to derive stellar masses and SFRs for our three galaxies. For consistency with the local MZR and FMR considered here (discussed in Section 4), we use a Chabrier (2003) stellar initial mass function (IMF).⁶ For the star-formation history (SFH), we assume a delayed-exponential form. We find for all three galaxies stellar masses and SFRs of $10^{8\text{--}9} M_\odot$ and $16\text{--}65 M_\odot \text{ yr}^{-1}$ (Table 2). Furthermore, the inferred stellar (and gas-phase⁷) metallicities are significantly subsolar ($12 + \log(\text{O}/\text{H}) = 7.25 \pm 0.21, 7.53 \pm 0.08, \text{ and } 7.50 \pm 0.12$) and an overall low attenuation ($A_V = 0.37 \pm 0.04, 0.50 \pm 0.03, \text{ and } 0.21 \pm 0.03$) for ID4590, ID6355, and ID10612, respectively. It is interesting that we obtain broad-band metallicities fairly consistent with the T_e ones but for ID6355 (which is underestimated by a factor of ~ 5), confirming in particular the very low metallicity of ID4590 (see Section 3.3).

⁴Available at <https://github.com/spacetelescope/jwst>.

⁵Available at <https://github.com/spacetelescope/webbpsf>.

⁶Arguably, this IMF may not be appropriate for these young, low-metallicity galaxies. However, it is not established what the correct IMF at such early times should be and an IMF conversion only introduces a constant scaling factor.

⁷In SED modelling, we assume that the stellar and gas-phase metallicity are the same.

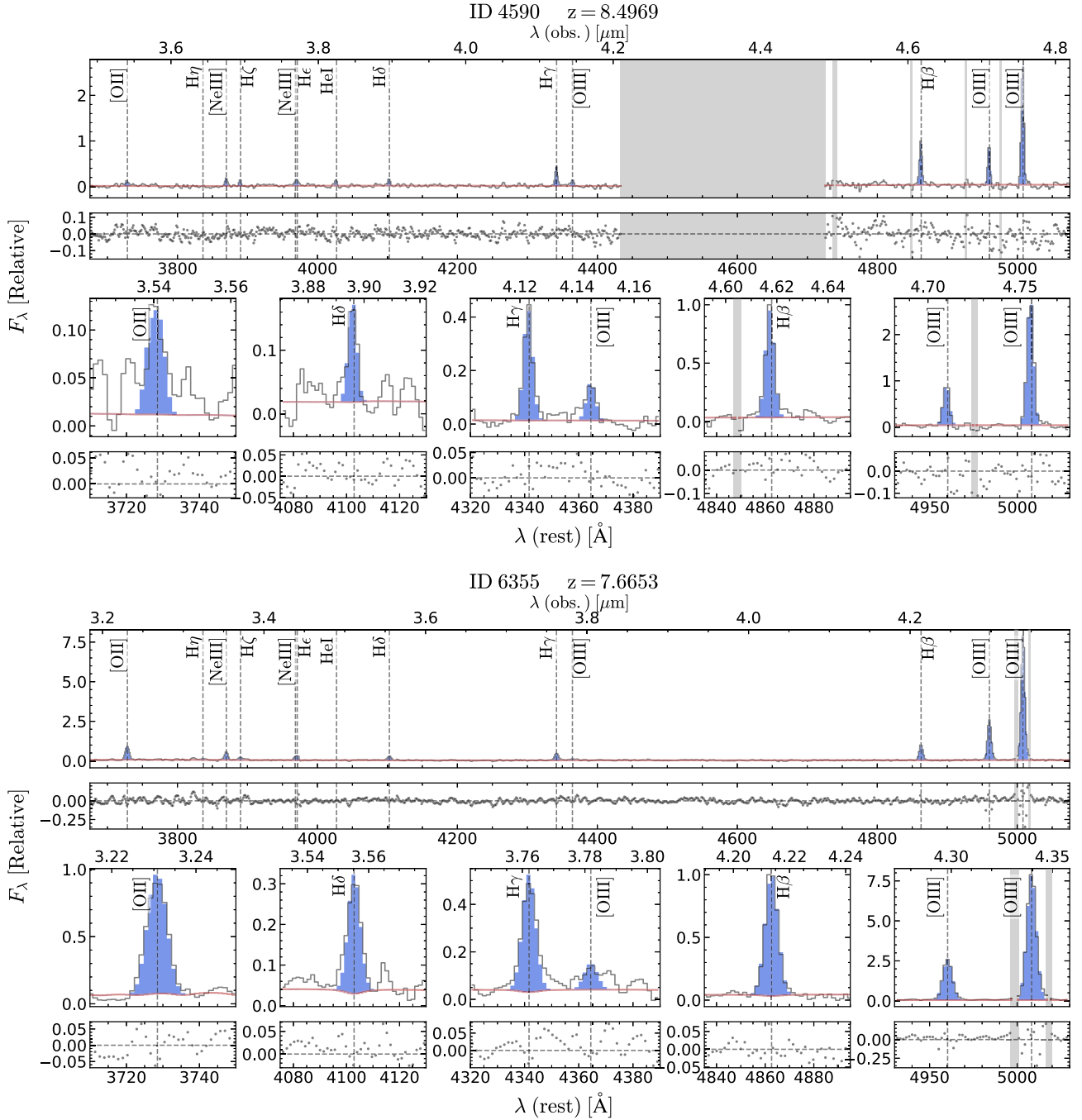


Figure 1. *JWST*/NIRSpec spectra of the three sources analysed in this work. Several Hydrogen, Helium, and metals emission lines are detected; the best-fitting models are highlighted in blue. The data and best-fitting continuum are traced by the solid grey and red lines, respectively; the dots are the residuals. The bottom panels show a zoom-in on the spectral region of three groups of lines; from left to right they are: the [O II] λ 3727, 29 doublet, H δ , H γ and [O III] λ 4363, and H β and [O III] λ 5007. The grey regions have been masked due to artefacts (either in the spectrum or in the noise) or sigma clipping; the wide grey region at 4450–4750 \AA in the top panel of ID 4590 falls in the detector gap.

Within the BEAGLE framework, we also explore a constant SFH, which has however little effect on the inferred stellar masses and SFRs. Finally, we explore two other SED fitting codes, namely BAGPIPES (Carnall et al. 2018) and PROSPECTOR (Johnson et al. 2021). We run PROSPECTOR with the same setup as in Tacchella et al. (2022). With BAGPIPES, we explored three alternative SFHs: either constant, delayed exponential, or delayed exponential with burst. Reassuringly, we find that the derived stellar masses and

SFRs are consistent within 1σ uncertainties between the different codes, as well as with those obtained by Tacchella et al. (2022) via a PROSPECTOR run including emission lines and assuming a bursty prior on the SFH. Moreover, the stellar masses (converted to the same IMF) agree within 1σ uncertainties with the results presented by Carnall et al. (2022). However, a more thorough comparison between these different SED fitting codes goes beyond the scope of this paper.

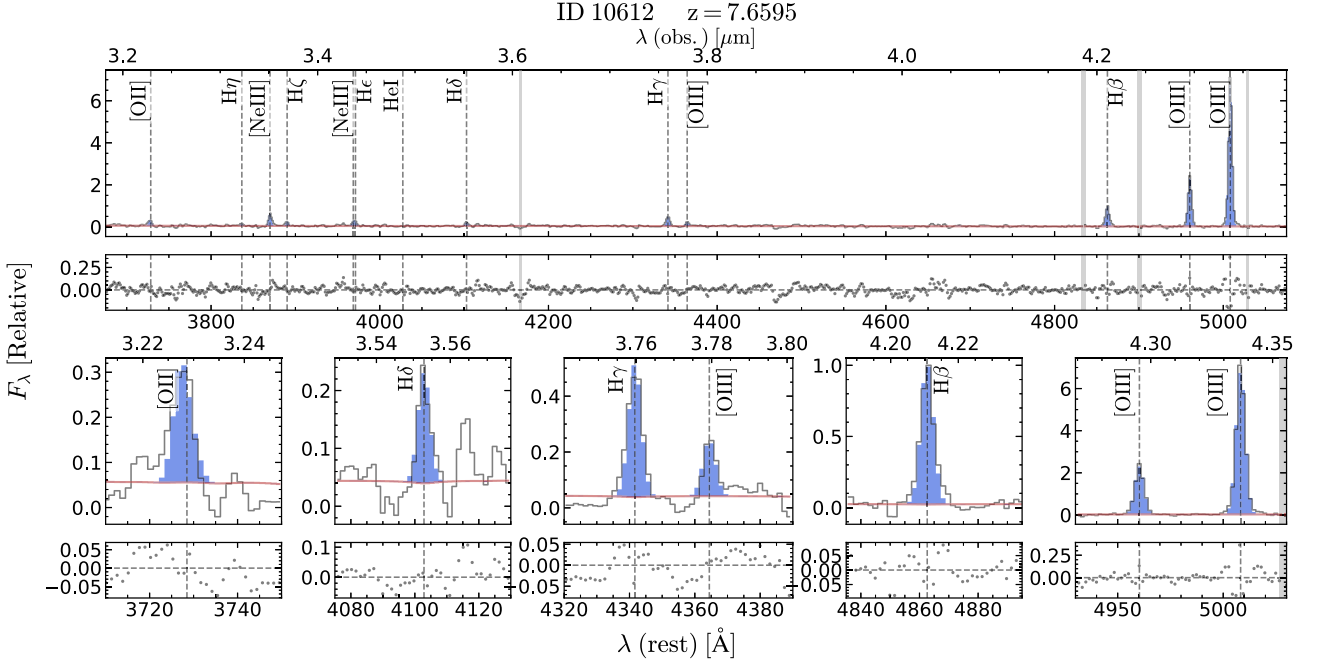


Figure 1. (continued)

Figure 1. (continued)

Table 1. Observed line intensities normalized to $H\beta = 1$ and errors on the ratio. The $H\beta$ emission line fluxes (in physical units of 10^{-18} erg s^{-1} cm^{-2}) measured from the spectra are as follows: ID 4590 = 1.54 ± 0.06 ; ID 6355 = 2.11 ± 0.05 ; ID 10612 = 1.19 ± 0.04 .

Galaxy ID	[O II] $\lambda\lambda$ 3727, 29	[Ne III] λ 3869	H ζ	H ϵ	H δ	H γ	[O III] λ 4363	[O III] λ 4959	[O III] λ 5007
4590	0.15 ± 0.07	0.17 ± 0.03	0.13 ± 0.02	0.13 ± 0.02	0.16 ± 0.02	0.41 ± 0.03	0.14 ± 0.02	0.96 ± 0.05	3.08 ± 0.13
6355	0.90 ± 0.10	0.45 ± 0.03	0.18 ± 0.02	0.18 ± 0.02	0.26 ± 0.02	0.46 ± 0.02	0.10 ± 0.02	2.66 ± 0.07	8.29 ± 0.21
10612	0.26 ± 0.08	0.50 ± 0.04	0.19 ± 0.03	0.14 ± 0.03	0.17 ± 0.03	0.44 ± 0.03	0.18 ± 0.03	2.34 ± 0.09	7.11 ± 0.24

Table 2. Derived galaxy properties.

Galaxy ID	4590	6355	10612
Redshift	8.496	7.665	7.658
μ^a	3.74 ± 0.07	1.231 ± 0.002	1.339 ± 0.003
$\log(M_*/M_\odot)^b$	7.75 ± 0.07	8.72 ± 0.04	8.08 ± 0.04
$\log(\text{SFR } (M_\odot \text{ yr}^{-1}))^b$	0.35 ± 0.07	1.47 ± 0.04	0.90 ± 0.04
A_V (nebular) ^c	$0.68^{+0.34}_{-0.25}$	$0.0^{+0.1}_{0.0}$	$0.40^{+0.46}_{-0.27}$
A_V (stellar) ^d	0.37 ± 0.04	0.50 ± 0.03	0.21 ± 0.03
T_e ([O III])(10^4 K)	2.77 ± 0.42	1.20 ± 0.07	1.75 ± 0.16
$12 + \log(\text{O}/\text{H})$	6.99 ± 0.11	8.24 ± 0.07	7.73 ± 0.12

Notes. ^a derived from the lens models presented in Mahler et al. (2022)

^b values are corrected for magnification (errors on μ are propagated)

^c inferred from ratios of Balmer lines

^d inferred from SED fitting

2.2.3 Magnification factors

The galaxies analysed in this paper are background galaxies of the SMACS J0723.3-7327 lensing cluster with publicly available lens models. In this work, we exploit the models recently provided by Mahler et al. (2022), which combine ancillary *HST* with novel *JWST*/NIRCAM data to better constrain the cluster mass distribution. Magnification maps are derived for each target redshift, and the average value from within a 1 arcsec-wide box around the central

coordinates of each galaxy is assumed as the fiducial magnification factor. The associated uncertainty is computed from the standard deviation of one hundred realizations of the magnification maps obtained through Monte Carlo simulations by perturbing the input model parameters. These results in the magnification factors listed in Table 2.

Additional models for this cluster have been recently published by Pascale et al. (2022) and Caminha et al. (2022). A full assessment of the systematics introduced by the adoption of different lensing models is far beyond the scope of this work. However we remark that, for the highest magnification galaxy ID4590, the different values obtained by the available models can impact the stellar mass and SFR determination for this source up to a factor of 30 – 50 per cent.

3 LINE RATIOS AND ABUNDANCES AT $z \sim 8$

3.1 Balmer decrements and dust attenuation

Fig. 2 shows a comparison between the observed and theoretical fluxes relative to $H\beta$ for different Balmer emission lines, namely $H\zeta$, $H\epsilon$, $H\delta$, and $H\gamma$. The theoretical values of the corresponding Balmer decrements computed using PYNEB (Luridiana, Morisset & Shaw 2012, 2015), assuming Case B recombination, an electronic temperature $T_e = 1.5 \times 10^4$ K and an electron density $N_e = 300 \text{ cm}^{-3}$ (i.e. $H\zeta/H\beta \approx 0.105$, $H\epsilon/H\beta \approx 0.159$, $H\delta/H\beta \approx 0.259$, $H\gamma/H\beta \approx$

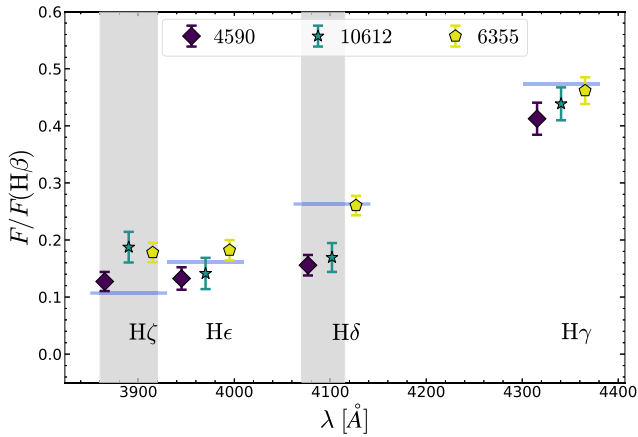


Figure 2. Flux ratios between different Balmer lines and the $H\beta$ as observed in all galaxies' spectra. The theoretical values expected from atomic physics (assuming the case B recombination at $T = 1.5 \times 10^4$ K and $N_e = 300 \text{ cm}^{-3}$) are marked by the blue lines. All observed ratios are consistent with little dust attenuation. The grey shaded areas mark regions with unreliable ratios: non-physical $H\zeta/H\beta$ ratio might be driven by $H\zeta$ flux being contaminated by He I emission, whereas residuals in the background subtraction may affect the $H\delta$ emission in ID4590 and ID10612.

0.468), are marked by the horizontal blue lines. Under realistic assumptions, these ratios are fairly insensitive to the precise physical conditions of the ISM. For example, varying the temperature between $T_e = 0.5 \times 10^4$ K and $T_e = 3 \times 10^4$ K and the density between $N_e = 10 \text{ cm}^{-3}$ and $N_e = 10000 \text{ cm}^{-3}$ would make these ratios change by at most ~ 3.5 per cent.

We note that while a poorly corrected stellar absorption could potentially bias the Balmer ratios, the continuum is nearly undetected in the spectra of these three galaxies. Moreover these are extremely young galaxies that are not expected to have significant Balmer absorption based on the level of continuum detection. While Balmer-line absorption is expected to be weaker for $H\beta$ than for $H\gamma$ and $H\delta$ at least, even assuming an equivalent width of 4 \AA for $H\beta$ absorption and 0 \AA for the other Balmer lines would lead to a correction of less than 5 per cent.

The Balmer ratios shown in Fig. 2 are consistent with the theoretical value, or slightly lower. The exceptions are $H\zeta$, for galaxies ID10612 and ID6355, however, $H\zeta$ is very faint and possibly contaminated by He I. The other exception is $H\delta$, which is significantly lower than the theoretical value for galaxies ID4590 and ID10612, while is well in agreement with the theoretical value for ID6355; however, the former two galaxies are those with the lowest S/N and, in addition, some background residual problems seem to be present at these wavelengths for these galaxies. We note that, as already reported by Schaerer et al. (2022), the use of the level 3 products from the MAST archive would result in Balmer ratios much higher than the theoretical values, confirming the presence of residual issues in the data processing and/or flux calibration suggested both in the *JWST* documentation⁸ and by the significant levels of spectrophotometric correction we had to introduce (see Section 2.1.2).

We simultaneously fit the ratios of $H\gamma/H\beta$ and $H\epsilon/H\beta$ to infer the dust attenuation by assuming the SMC curve from Gordon et al. (2003) with $R_V = 2.505$; as mentioned, $H\delta/H\beta$ appears strongly underestimated in both ID4590 and ID10612 compared to the other

two Balmer decrements at fixed attenuation, possibly due to poor continuum subtraction, hence we consider this ratio only for ID6355. The inferred values of nebular A_V for the three sources are reported in Table 2. The use of the locally derived Gordon et al. (2003) SMC curve may be arguable for such distant galaxies, however it as been shown to be adequate for $z \sim 2$ low-metallicity galaxies (Shivaei et al. 2020). Moreover, since the $[\text{O III}]\lambda 4363$ emission line is close in wavelength to the $H\gamma$ line and $[\text{O III}]\lambda 5007$ is close to $H\beta$, and considering that the attenuation is mostly driven by $H\gamma/H\beta$, the choice of the attenuation curve has a minor effect on the dust-corrected value of the $[\text{O III}]\lambda 4363/[\text{O III}]\lambda 5007$ line ratio (and hence on the inferred temperature and metallicity).

We compare the nebular attenuation to the attenuation of the continuum derived from the BEAGLE SED fitting, once scaling stellar to nebular attenuation by a factor of 2.11,⁹ following Shivaei et al. (2020). We find agreement within the uncertainties for ID4590 and ID10612, whereas a significantly higher attenuation from the SED fitting in ID6355.

3.2 Excitation diagnostics

At the redshifts of our targets $H\alpha$ and adjacent nebular lines are shifted outside the NIRSpect band, so they cannot be used to construct the classical BPT diagnostic diagrams (Baldwin, Phillips & Terlevich 1981). However, interesting information about the excitation properties of these sources can be inferred from the $[\text{O III}]\lambda 5007/H\beta$ versus $[\text{O II}]\lambda 3727, 29/H\beta$ diagram. This diagram is shown in the left-hand panel of Fig. 3, where the shaded region marks the distribution of local galaxies in the MPA-JHU catalogue from the Sloan Digital Sky Survey (Brinchmann et al. 2004; Tremonti et al. 2004) and other surveys at $z \sim 1-3$ (Troncoso et al. 2014; Onodera et al. 2016; Sanders et al. 2021; Hayden-Pawson et al. 2022). The dashed line indicates the local dividing line between star-forming galaxies and active galactic nuclei (AGNs) identified by Lamareille (2010).

Intermediate-redshift star-forming galaxies are characterized by a large scatter, but they also tend to be shifted towards higher values of $[\text{O III}]/H\beta$. This is an effect similar to that seen in the classical BPT diagram (see the discussion in Maiolino & Mannucci 2019), which has been attributed to a combination of higher ionization parameter and harder radiation field associated with α -enhanced stellar populations (e.g. Strom et al. 2018; Topping et al. 2020, but see also Curti et al. 2022). Therefore, finding that the two galaxies at $z \sim 7.6$ are located above Lamareille (2010)'s line does not necessarily imply that these are AGNs, but that they follow the same trend as intermediate-redshift galaxies.

Galaxy ID4590 at $z \sim 8.5$ is located in a region of the diagram poorly populated by both local and intermediate-redshift galaxies, with $\log([\text{O III}]/H\beta) \sim 0.5$ and $\log([\text{O II}]/H\beta) \sim -0.75$. According to the photoionization models presented in Nakajima & Maiolino (2022), and shown in Fig. 4, this region is populated by young, metal-poor galaxies. However, we also note that the presence of an AGN with low metallicity ($Z \sim 10^{-3}$) cannot be completely ruled out by these models.

The right-hand panel of Fig. 3 shows instead the excitation diagram $O_{32} = [\text{O III}]\lambda 5007/[\text{O II}]\lambda 3727, 29$ versus $R_{23} = ([\text{O III}]\lambda 4959, 5007 + [\text{O II}]\lambda 3727, 29)/H\beta$, where the same local and intermediate-redshift galaxies are shown as in the left-hand panel. This diagram can be considered as a proxy of ionization parameter (primarily traced by O_{32} ; Díaz et al. 2000) versus metallicity (primarily traced by R_{23} , e.g.

⁸see <https://jwst-docs.stsci.edu/jwst-calibration-pipeline-caveats>

⁹we note the exact determination of this factor is quite uncertain

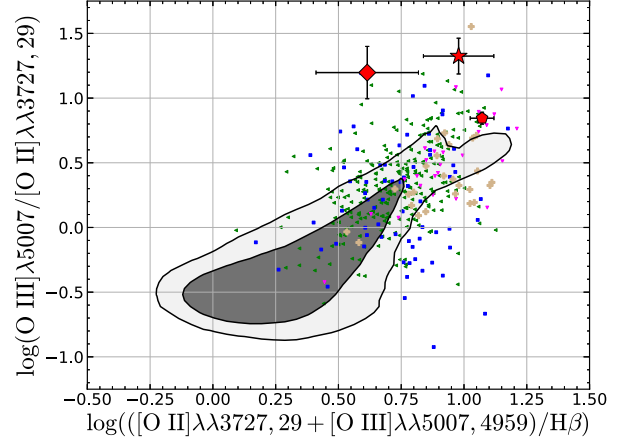
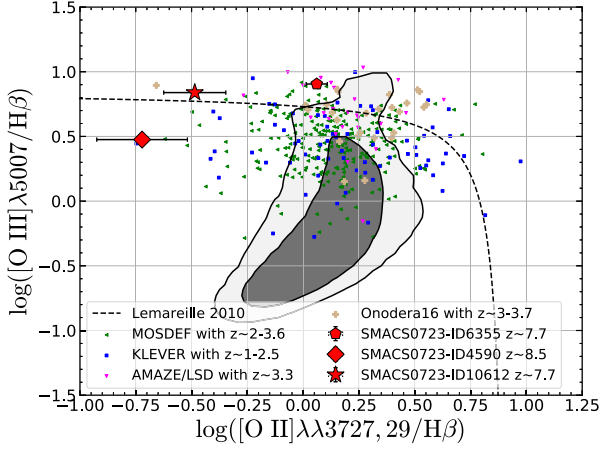


Figure 3. $[\text{O III}]/\text{H}\beta$ versus $[\text{O II}]/\text{H}\beta$ diagram (left-hand panel) and $[\text{O III}]/[\text{O II}]$ versus R_{23} diagram (right-hand panel) for local SDSS galaxies (grey contours marking the 70 per cent and 90 per cent of the distribution), galaxies at $z \sim 1-3$ from the literature, and the *JWST* sample at $z \sim 8$.

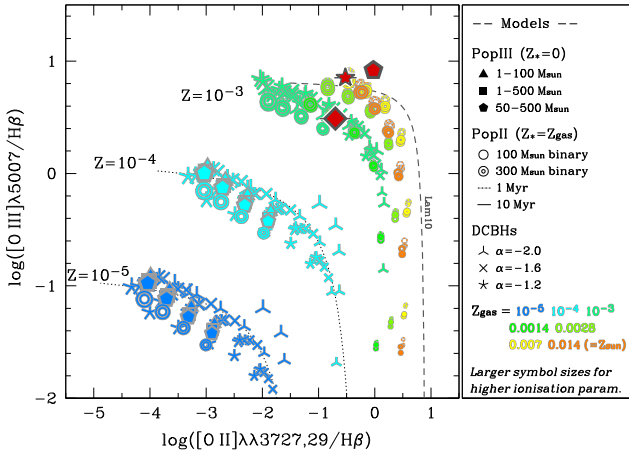


Figure 4. $[\text{O III}]/\text{H}\beta$ versus $[\text{O II}]/\text{H}\beta$ diagram illustrating the photoionization models for low metallicity PopII, PopIII, and AGNs from Nakajima & Maiolino 2022. Different symbols mark different population of objects (as explained in the legend), while different colours belong to different values of the gas-phase metallicity. The line ratios observed in our $z \sim 8$ galaxies are marked with red symbols.

Nagao, Maiolino & Marconi 2006). However, high O_{32} values are sometimes also considered as indicative of density-bounded clouds, possibly associated with high escape fractions (f_{esc}) of Lyman-continuum (LyC) photons (Nakajima & Ouchi 2014; Barrow et al. 2020; Nakajima et al. 2020). All three galaxies at $z > 7$ considered here have very high values of O_{32} . Especially, ID10612 at $z = 7.6$ and ID4590 at $z = 8.5$ have extremely high values of O_{32} that are rarely seen even in galaxies at $z \sim 2-3$, if not in extreme $[\text{O III}]\lambda 5007$ emitters with very high equivalent widths (Tang et al. 2019). The fact that these galaxies have such high values of O_{32} can potentially indicate very high ionization parameters and/or large LyC escape fractions (Chisholm et al. 2022). Based on Ly α emitters (LAEs) probed by different low- and intermediate-redshift galaxy surveys with similar line ratios and metallicities to our *JWST* sample we can provide (following e.g. Izotov et al. 2018b; Nakajima et al. 2020) a rough estimate of the f_{esc} in our galaxies. In particular, the O_{32} value for ID6355 ($\log \text{O}_{32} = 0.96$) is consistent with LyC leakers with $f_{\text{esc}} \lesssim 0.1$, whereas ID4590 and ID10612 show O_{32} values ($\log \text{O}_{32} = 1.18; 1.36$, respectively) comparable with f_{esc} from ~ 0.1

up to ~ 0.5 . We stress however that the relationship between O_{32} and f_{esc} is quite scattered, and that a large O_{32} may be a necessary but not sufficient condition for the presence of relevant LyC emission (Izotov, Thuan & Guseva 2017).

3.3 Oxygen abundance determination

We exploit the highly significant detection of the $[\text{O III}]\lambda 4363$ auroral line in *JWST*/NIRSpec spectra of the three galaxies studied here to measure the oxygen abundance (a proxy of the total gas-phase metallicity) by means of the electron-temperature (T_e) method. More specifically, $[\text{O III}]\lambda 4363$ is detected at 8.6σ , 7.3σ , and 6.4σ in the spectra of ID4590, ID10612, and ID6355, respectively.

For the purposes of temperature and abundance computation, we model each galaxy as a single H II region constituted by two ionization zones: the high-ionization one, traced by the O^{++} ion; and the low-ionization one, traced by the O^+ ion. We have direct access to the temperature of the high-ionization zone (t_3) from the ratio between the $[\text{O III}]\lambda 4363$ and $[\text{O III}]\lambda 5007$ emission lines.

We implement the iterative procedure described in Nicholls et al. (2013) to infer t_3 from this auroral-to-nebular diagnostic line ratio, adopting the atomic data from Palay et al. (2012), and assuming an electron density $N_e = 300 \text{ cm}^{-3}$ (a value typically measured in the ISM of $z \sim 2-3$ galaxies, e.g. Sanders et al. 2016); different values of N_e would not impact significantly our results, as the $[\text{O III}]\lambda 4363/[\text{O III}]\lambda 5007$ ratio depends only mildly on gas density. The derived t_3 temperatures for our galaxies are reported in Table 2. The temperatures derived for ID10612 and ID6355 ($\sim 17\,600 \text{ K}$ and $\sim 12\,200 \text{ K}$) are consistent with the typical values of low- and intermediate-metallicity H II regions, whereas the ID4590 source at $z \sim 8.5$ is characterized by a much higher temperature ($\sim 28\,600 \text{ K}$), possibly driven by low metallicity and high ionization parameter, and similar to what observed in local extremely metal-poor galaxies (e.g. Izotov et al. 2018a; Izotov, Thuan & Guseva 2021).

Since we do not have access to temperature diagnostics for the low-ionization species (i.e. no auroral line emission is detected from N^+ or S^+ species in the spectra), here we adopt the temperature-temperature relation from Pilyugin et al. (2009) to infer the temperature of the low-ionization zone (t_2): $t_2 = 2640 + 0.835 \times t_3$. While the applicability of such relation at $z \sim 8$ is questionable, adopting a different locally calibrated t_2 - t_3 relation does not significantly impact the total oxygen abundance determination since

in these low-metallicity environments the O^{++} abundance is largely dominant over O^+ (Andrews & Martini 2013; Curti et al. 2017). For comparison, adopting the t_2 – t_3 relation from Garnett (1990) impacts the final metallicity calculation by less than 1 per cent.

Finally, we compute the ionic abundances of O^+ and O^{++} using the *getIonAbundance* routine of PYNEB (v 1.1.10, Luridiana et al. 2012, 2015, adopting the atomic data from Palay et al. 2012), which provides the abundance of ionic species given the electron temperature (of the corresponding ionization zone), the gas density, and the flux of a strong emission line (e.g. $[O\text{III}]\lambda 5007$ for O^{++} , $[O\text{II}]\lambda 3727$, 29 for O^+) relative to $H\beta$, and assuming the same atomic data from Palay et al. (2012). Here, we assume that the total oxygen abundance is the sum of the abundances of the singly and doubly ionized oxygen species, i.e. $O/H = O^+/H + O^{++}/H$, neglecting contributions from higher ionization states.

The derived electron temperatures and oxygen abundances for our galaxy sample are reported in Table 2; uncertainties on both quantities are computed through Monte Carlo simulations by randomly perturbing (assuming a Gaussian noise distribution) one hundred times all measured line fluxes by their measurement errors¹⁰ (including the uncertainty from reddening correction), randomly varying the density between 100 and 1000 cm^{-3} , and repeating the full temperature and abundance calculation for each iteration, taking the standard deviation of the distribution of temperatures and abundances obtained as the representative uncertainties on the measured values. None the less, we note that these values probably underestimate the true uncertainties, because the systemic contributions are not considered. In particular, temperature stratification in H II regions can significantly halter the derived metallicity (Stasinska 2002; Kewley, Nicholls & Sutherland 2019).

As briefly mentioned above, the high t_3 measured in ID4590 places this object at the limit of what has ever been observed in the local Universe for star-forming galaxies. Such high temperature might also reveal the presence of a much harder ionizing continuum associated with AGN activity (Dors et al. 2021; Riffel et al. 2021; but see also Katz et al. 2022 for different possible interpretations), which is indeed not ruled out also by photoionization models, as already shown by comparing the observed line ratios with the predictions of the Nakajima & Maiolino (2022) models in Fig. 4. Although we favour the scenario of star-forming galaxy with low metallicity and high ionization parameter, for comparison we verified that the analytic approach presented in Dors et al. (2021, equations 9 and 10), tuned for deriving T_e -based metallicities in AGNs, provides a comparable estimate of the total oxygen abundance, finding temperatures and metallicities consistent within the uncertainties with our fiducial T_e -method. We simply note that, in case of the presence of an AGN, the metallicity of ID4590 might be underestimated by not accounting for the abundance of the O^{+++} species, and that the stellar mass and SFR determination would require further care in decomposing the stellar from the AGN contribution to the photometry. However, we also note that obscuration from the dusty tori in type II AGNs could weaken the $[O\text{III}]\lambda 4363$ emission (e.g. Nagao, Murayama & Taniguchi 2001).

It is also interesting to note that the galaxy with the lowest metallicity, ID4590, is also the one with the highest dust attenuation. While one should not overinterpret this result, as the uncertainty on attenuation is large, this is something that is observed in some local dwarf, low metallicity galaxies (e.g. SBS 0335-052), which can have

large dust masses and high dust attenuation. At a given gas mass, compactness and geometrical effect can strongly contribute to the higher dust attenuation; moreover, high gas density can foster the rapid growth of dust in the ISM (Schneider, Hunt & Valiante 2016).

Finally, we note that, in a recent paper, Schaerer et al. (2022) analyses the same three galaxies, obtaining different results in terms of gas temperature and metallicity. They notice non-physical Balmer decrements in their spectra, and apply a power-law, wavelength-dependent correction. They also infer un-physically high temperature for ID4590. As discussed in the previous sections, we obtain reasonable Balmer decrements, without introducing any a posteriori adjustment, and we can reliably measure the temperature in ID4590, which gives results consistent with the ISM properties of extremely metal-poor galaxies. We believe that these differences can be ascribed to our additional processing of the data, as discussed in detail in Section 2.1.2. We note that similar issues have been reported, discussed, and addressed with different prescriptions also by other recent works (Arellano-Córdova et al. 2022; Brinchmann et al. 2022; Rhoads et al. 2022; Taylor et al. 2022; Trump et al. 2022).

3.4 Comparison with strong-line metallicity calibrations

Metallicity diagnostics based on strong nebular emission-line ratios are widely adopted by the astronomical community to infer the chemical abundances of large samples of galaxies, for which auroral lines are often not detected. Several authors have calibrated such diagnostics by exploiting samples of local star-forming galaxies and H II regions with T_e -based metallicity determinations (e.g. Pettini & Pagel 2004; Maiolino et al. 2008; Marino et al. 2013; Pilyugin & Grebel 2016; Curti et al. 2017; Bian et al. 2018; Sanders et al. 2021). However, an evolution in the ISM conditions of high-redshift galaxies compared to the local Universe might impact the intrinsic dependence of strong-line ratios on gas-phase metallicity, potentially hampering their use as abundance diagnostics at high redshift and thus biasing the assessment and interpretation of the chemical evolution history of galaxies.

Here, we exploit the T_e -based abundances delivered by *JWST*/NIRSpec spectra to test the rest-frame optical, strong-line metallicity calibrations for the first time at $z \sim 8$. In Fig. 5, the T_e -based $\log(O/H)$ measurements of the three galaxies in our sample are plotted against some of the most widely adopted strong-line metallicity diagnostics, specifically: $R_3 = [O\text{III}]\lambda 5007/H\beta$, $R_2 = [O\text{II}]\lambda 3727, 29/H\beta$, $R_{23} = ([O\text{III}]\lambda 4959, 5007 + [O\text{II}]\lambda 3727, 29)/H\beta$, $O_{32} = [O\text{III}]\lambda 5007/[O\text{II}]\lambda 3727, 29$, and $Ne_{3O2} = [Ne\text{III}]\lambda 3869/[O\text{II}]\lambda 3727, 29$.

Different calibration curves (in the form of polynomial relations between metallicity and strong-line ratios) are shown for these diagnostics in each panel, namely from Maiolino et al. (2008) Curti et al. (2020a), Sanders et al. (2021), Bian et al. (2018), and Nakajima et al. (2022). In brief, Curti et al. (2020a) complemented the Curti et al. (2017) calibrations based on T_e metallicity measurements performed on stacked spectra of SDSS galaxies in the $[O\text{II}]\lambda 3727, 29/H\beta$ versus $[O\text{III}]\lambda 5007/H\beta$ diagram; here, we also include a new calibration of the Ne_{3O2} diagnostic based on the same methodology and combined sample of stacks and individual SDSS galaxies with $[O\text{III}]\lambda 4363$ detections described in Curti et al. (2017), and which was not published before.¹¹ Sanders et al. (2021) combined the measurements performed by Andrews & Martini (2013) in stellar mass (M_*)–SFR

¹⁰We verified that errors from the PPF fitting procedure are consistent with those inferred from bootstrapping

¹¹The calibration is presented in the usual form $[\log(R) = \sum_{i=0}^n a_i x^i]$, where $x = 12 + \log(O/H) - 8.69$ (solar metallicity from Allende Prieto, Lambert &

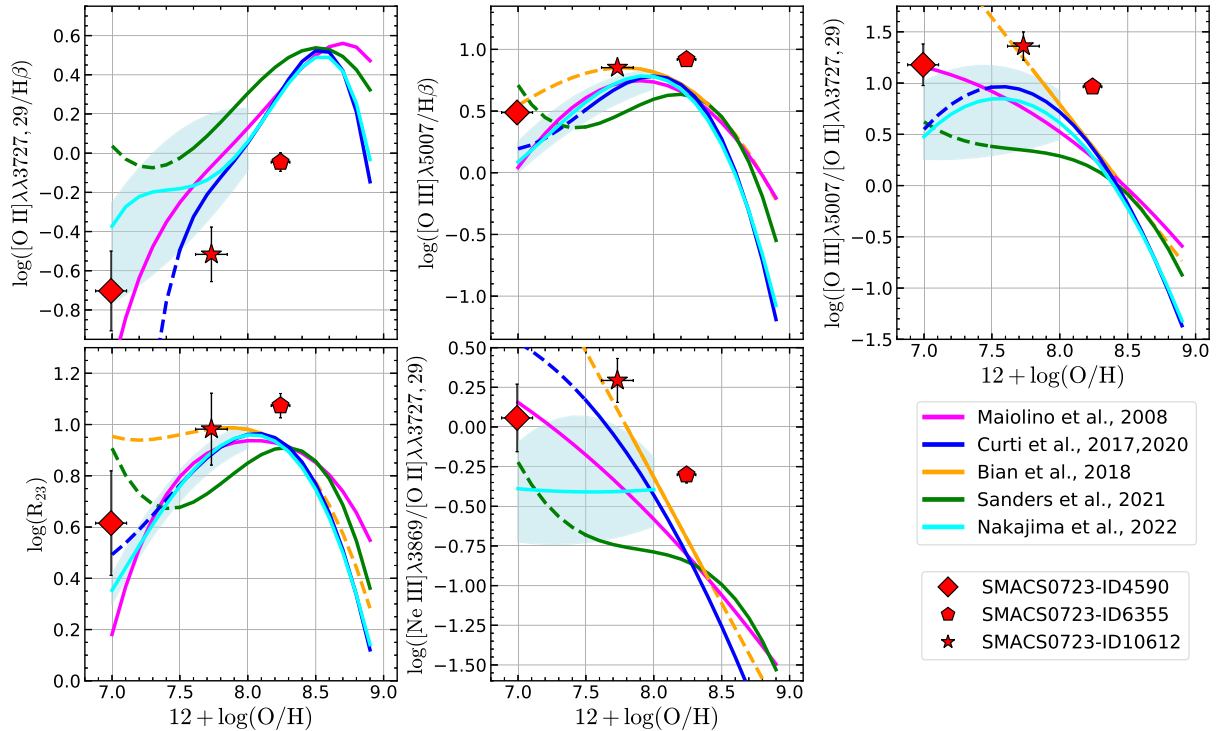


Figure 5. The relationships between T_e metallicity and strong-line ratios for the *JWST* galaxy sample are compared with some widely adopted abundance calibrations, namely from Maiolino et al. (2008), Bian, Kewley & Dopita (2018), Curti et al. (2017, 2020a), Sanders et al. (2021), and Nakajima et al. (2022). All these calibration relations are built from samples of local star-forming galaxies with T_e -based measurements, but are based on slightly different assumptions (see the text for more details). The solid lines represent the relationships in the metallicity calibration range as provided by the authors, whereas dashed lines mark extrapolations of the polynomial fit outside that range. The shaded areas encompass the region between the calibrations based on the low- and high-EW($H\beta$) subsamples of metal-poor galaxies as presented in Nakajima et al. (2022).

stacks of SDSS galaxies with a sample of low-metallicity dwarfs from Berg et al. (2012), whereas Maiolino et al. (2008) combined a sample of galaxies with auroral line detections at low metallicity from Nagao et al. (2006) with predictions from photoionization models in the high-metallicity regime. Nakajima et al. (2022) instead extended the calibrations based on the Curti et al. (2017) SDSS stacks to the low-metallicity regime leveraging T_e -measurements in extremely metal-poor galaxies from the EMPRESS survey (Kojima et al. 2020); in particular, in Fig. 5 we show the calibrations best-fit obtained by Nakajima et al. (2022) from the full galaxy sample with the solid line, whereas the shaded areas encompass the region between the calibrations based on the subsamples of metal-poor galaxies characterized by high- and low-EW($H\beta$) (i.e. $\text{EW}(H\beta) > 200 \text{ \AA}$ and $< 100 \text{ \AA}$, respectively). Finally, Bian et al. (2018) built a set of calibrations on a sample of local analogues of high-redshift galaxies (for which auroral lines are detected in stacked spectra), selected to match the location of observed $z \sim 2$ sources in the [N II]–BPT diagram (Shapley et al. 2015; Strom et al. 2017); such calibrations, though still based on local galaxies, are thus specifically built for being applied to high-redshift galaxy spectra.

The two $z \sim 7.6$ sources, ID10612 and ID6533, present a higher level of nebular excitation than lower redshift calibration samples, placing them above the upper plateau of R23, R3, and O32 curves, and below the expected R2 value at given metallicity, in the Curti

et al. (2020a), Maiolino et al. (2008), Nakajima et al. (2022), and Sanders et al. (2021) calibrations, whereas the Bian et al. (2018) curves better cover that region of the line ratios parameter space. The extremely metal-poor $z \sim 8.5$ ID4590 source, instead, is located in a region outside the validity range of most calibrations under study; none the less, it exhibits line ratios properties resembling those of extremely metal-poor galaxies in the local Universe, and especially Maiolino et al. (2008) and Nakajima et al. (2022) calibrations, as well as some of the extrapolations of Curti et al. (2020a) and Sanders et al. (2021) curves (shown as dashed lines¹²), provide a reasonable match to most of the line ratios observed in this galaxy.

Some of the observed deviations are actually still within the scatter of the calibration relations (typically ranging between 0.1 and 0.2 dex in a given line ratio at fixed metallicity, depending on the diagnostic and the calibration sample). In Table 3, we compare the observed and predicted (given the measured metallicity) line ratios for each considered strong-line diagnostics (i.e. the vertical offset from the calibration relation), and report the significance of the deviation (in units of σ) taking into account both measurements uncertainties and the intrinsic dispersion of each individual calibration.¹³ In many cases, the measurements clearly fail to simultaneously match all the

¹²It should be stressed that sometimes high-order polynomials express non-physical behaviours outside their fitting range

¹³Since Bian et al. (2018) do not provide an estimate of the dispersion of the calibrations, we assume a typical dispersion of 0.15 dex for all diagnostics. We further note that in some cases, e.g. the Ne III O_2 calibration from Nakajima et al. (2022), a very large intrinsic dispersion of the calibration may artificially

Asplund 2001), and the best-fitting coefficients are: $c_0 = -1.632$; $c_1 = -2.061$; $c_2 = -0.461$.

Table 3. Significance of the deviation (in units of σ) of the observed line ratios in the *JWST* $z \sim 8$ galaxy sample from the predictions of each of the strong-line calibrations presented in Fig. 5. Both the measurements uncertainties on the line ratios and the intrinsic dispersion of the calibrations (σ_{cal} , reported here as provided by the various authors) are taken into account.

Galaxy ID	R2	R3	O32	R23	Ne3O2
Maiolino et al. (2008)					
σ_{cal}	0.10	0.10	0.20	0.06	0.06
4590	1.68	3.03	0.08	1.77	0.39
6355	2.31	1.88	4.39	0.96	3.16
10612	2.20	0.86	2.97	0.41	3.18
Curti et al. (2017, 2020a)					
σ_{cal}	0.11	0.09	0.15	0.06	0.12
4590	14.94	3.22	2.54	0.59	1.97
6355	2.99	2.62	3.80	1.80	3.82
10612	1.89	1.80	2.11	0.64	2.04
Bian et al. (2018)					
σ_{cal}^1	–	–	–	–	–
4590	–	0.35	5.23	1.34	4.7
6355	–	1.50	3.71	0.95	2.52
10612	–	0.01	0.57	0.004	0.91
Sanders et al. (2021)					
σ_{cal}	0.13	0.10	0.19	0.08	0.20
4590	3.10	2.31	1.98	1.37	0.92
6355	3.65	2.86	4.05	1.77	2.64
10612	3.29	3.86	4.32	1.49	4.28
Nakajima et al. (2022)					
σ_{cal}	0.27	0.16	0.39	0.10	0.42
4590	0.95	2.54	1.62	1.18	0.95
6355	1.26	1.75	1.72	1.38	0.18
10612	1.29	0.74	1.32	0.53	1.58

Note. ¹ For Bian et al. (2018) we assume a dispersion of 0.15 dex on each calibration.

relations, prompting for a self-consistent revision of the calibrations at such early epochs which could be applied to galaxy spectra at different redshifts and/or observed in different filters, hence probing different emission lines.

4 COSMIC EVOLUTION OF THE METALLICITY SCALING RELATIONS

4.1 The mass–metallicity relation

In this section, we investigate the evolution in the metallicity scaling relations of galaxies as probed by the T_e -based O/H measurements enabled by *JWST*/NIRSpec at $z \sim 8$. In Fig. 6, we plot the three galaxies analysed in this paper on the mass–metallicity plane, along with the local relation inferred for the SDSS sample by Curti et al. (2020a) from T_e -based calibrations (contours in grey, best-fitting MZR in black). Compared to the MZR in the local Universe probed by SDSS galaxies, galaxies at $z \sim 8$ appear metal deficient at fixed stellar mass, in agreement with the expected redshift evolution of the MZR (see Maiolino & Mannucci 2019, and references therein). More specifically, ID6355 is offset by 0.18 dex from the $z \sim 0$ MZR, whereas ID10612 is offset by 0.52 dex. We also compare these observations at $z \sim 8$ with the MZR at $z \sim 2$ and $z \sim 3.3$, here

lower the significance of the computed deviation, which is therefore not a good representation of the calibration accuracy.

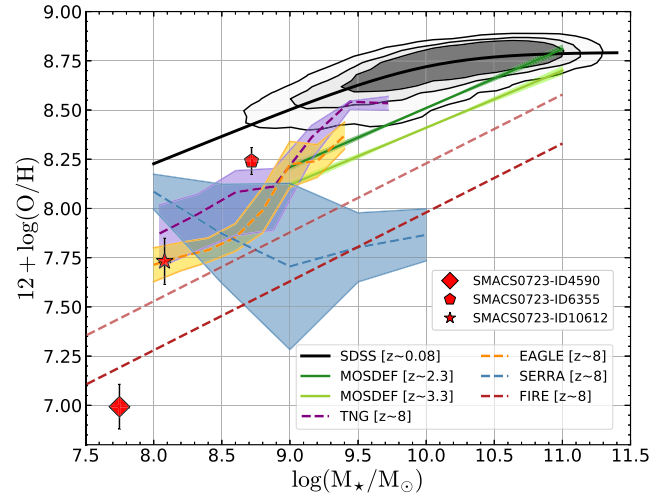


Figure 6. Mass–metallicity relation (MZR) for the *JWST* sample. The MZR for SDSS galaxies from Curti et al. (2020a) and its best-fit are shown by the grey contours and black curve, respectively. The best-fit to stacked spectra of MOSDEF galaxies from Sanders et al. (2021) (based on the Bian et al. 2018 calibrations tuned for high- z) are shown as representative for the MZR at $z \sim 2.3$ and $z \sim 3.3$. Moreover, the MZR at $z \sim 8$ predicted by TNG (Nelson et al. 2019), EAGLE (Schaye et al. 2015), FIRE (Ma et al. 2016) (extrapolated to $z = 8$), and SERRA (Pallottini et al. 2022) simulations are shown as dashed purple, orange, brown (light brown for re-scaled relation to match both local and $z = 2-3$ observations) and blue lines, respectively, with the shaded areas marking the region between the 16th and 84th percentiles of the predicted relation.

parametrized by a linear regression fit performed on stacked spectra from the MOSDEF survey as presented in Sanders et al. (2021). These authors adopt the Bian et al. (2018) T_e -empirical calibrations based on local analogues of high- z galaxies in order to reduce the potential biases affecting the use of local strong-line metallicity diagnostics at high redshift. Extrapolating the Sanders et al. (2021) relation to the low-mass range, we find that the metallicity of ID6355 is broadly consistent with the $z \sim 2.2$ MZR, whereas ID10612 is offset by 0.12 dex from the $z \sim 3.3$ MZR extrapolation. Naively, this could be interpreted as a signature of little or no evolution of the low-mass end of the MZR (either in slope or normalization) between $z \sim 3.3$ and $z \sim 7.6$, possibly implying a mild cosmic evolution in both the gas fraction (and consequent metal dilution) and the metal-loading factor of star-formation-driven outflows over ~ 1.2 Gyr (Sanders et al. 2021).

In contrast, we find that galaxy ID4560 is more than 1 dex offset from the $z \sim 0$ MZR, and deviates strongly (~ 0.8 dex) also from the extrapolation of the MZR at $z \sim 3.3$. Rather than very rapid redshift evolution of the MZR, this could indicate that ID4560 is in a very early evolutionary stage, in the process of rapidly building up its metals and approaching the MZR within a timeframe of just a few tens Myr (e.g. fig. 11 in Maiolino et al. 2008). Alternatively, this finding could indicate that the slope of the MZR becomes steeper at very low masses (not probed by the $z \sim 2.2-3.3$ surveys).

4.2 The fundamental metallicity relation

In this section, we explore whether these galaxies at $z \sim 8$ are consistent with the fundamental metallicity relation (FMR), which (as discussed in the introduction) describes the correlation between metallicity, stellar mass, and SFR, observational consequence of the interplay between gas accretion, star formation, and outflows

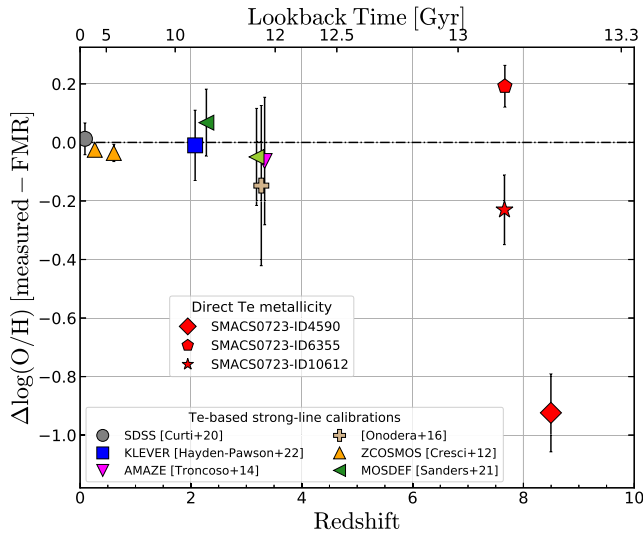


Figure 7. Deviations in the observed $\log(\text{O}/\text{H})$ from the predictions of the local fundamental metallicity relation (FMR; from Curti et al. 2020a, equation 5), plotted as a function of redshift (look back time is reported on the top axis). High-redshift galaxies with T_e -based measurements from *JWST*/NIRSpec are shown as red symbols. The average (and standard deviation) offset computed for different data sets compiled from the literature at different redshifts are also shown for comparison. All metallicities from the literature samples are self-consistently re-computed adopting the T_e -based (Curti et al. 2020a) calibrations at $z < 1$ and (Bian et al. 2018) at $z > 1$. At $z \sim 8$, galaxies appear offset from the predictions of the local FMR (though with different levels of significance), suggesting that they are far from the smooth equilibrium between chemical enrichment and gas flows that sets the average scaling relations in local galaxies (and up to $z \sim 3$).

which govern the secular evolution of galaxies, and which was found not to evolve (or marginally evolve), out to $z \sim 3$. Fig. 7 shows the deviation of the measured galaxy metallicities from the predictions of the FMR, as parametrized by equation (5) of Curti et al. (2020a). Different samples with available rest-frame optical spectroscopy compiled from the literature at various redshifts are included in the attempt to trace the cosmic evolution of this scaling relation across almost the entire history of the Universe. Specifically, these galaxies are compiled from Cresci et al. (2012; zCOSMOS at $z \sim 0.3$ –0.6), Hayden-Pawson et al. (2022; KLEVER at $z \sim 2.2$), Sanders et al. (2021; MOSDEF at $z \sim 2.3$ –3.3), Onodera et al. (2016; $z \sim 3.3$), and Troncoso et al. (2014; AMAZE at $z \sim 3.3$). The metallicities of galaxies at $z > 1$ have been consistently re-computed adopting the Bian et al. (2018) T_e -based strong-line calibrations (to account for potential evolution in the diagnostics), whereas we adopt the Curti et al. (2020a) calibrations for SDSS and zCOSMOS galaxies. For comparison, adopting instead the Curti et al. (2020a) calibrations for all galaxy samples produces, on average, a ~ 0.1 dex lower metallicity in $z \sim 2$ –3 galaxies. The various symbols in Fig. 7 mark, for each considered literature data set, the average offset in O/H (and standard deviation as errorbars) from the FMR predictions for individual galaxies within the sample. The red symbols mark instead individual T_e -based measurements for the *JWST* galaxy sample at $z \sim 8$; the errorbars on such datapoints are obtained by co-adding in quadrature the uncertainty on the $\log(\text{O}/\text{H})$ measurement from the T_e method and the uncertainty on the metallicity predicted by the FMR, evaluated from the standard deviation of the distribution of metallicities obtained by varying one hundred times the input M_* and SFR of galaxies within their errors.

The two galaxies at $z \sim 7.6$ show offsets of about ~ 0.2 dex (significant at $\sim 2\sigma$) from the FMR, though with different signs, suggesting different evolutionary stages. However, we also note that considering additional sources of uncertainty, like the errors associated to the parametrization of the functional form of the FMR and its extrapolation to the average M_* and SFR of the *JWST* sample (i.e. ~ 0.25 dex uncertainty, cfr. fig. 11 in Curti et al. 2020a), or the systematics introduced by the existence of temperatures stratification biasing the T_e -derived metallicity (Kewley et al. 2019), would make the two $z \sim 7.6$ galaxies broadly consistent with the FMR predictions.

The situation is readily different for the $z \sim 8.5$ source ID4590, which is observed to be much more metal-poor than the other two. This galaxy falls at the very low-mass, low-metallicity end of the MZR in Fig. 6 and is also offset by ~ 0.9 dex from the metallicity expected by the FMR given its M_* and SFR, a deviation significant at $\sim 6\sigma$ ($> 3\sigma$ even accounting for uncertainties on the FMR extrapolation). Considering that only ~ 100 Myr separate the two epochs (i.e. $z \sim 7.6$ and $z \sim 8.5$), this suggests that this object might be observed very far from the equilibrium between chemical enrichment and gas flows, and it is likely experiencing an initial, steeply rising phase of enrichment (see discussion in previous section) while being swamped by accretion of pristine gas. In agreement with the emission-line properties already discussed in terms of the metallicity calibration plots, the properties of this object resemble those of extremely metal-poor galaxies observed in the local Universe, which indeed have been long considered as potential analogues of galaxies in the epoch of reionization (e.g. Izotov et al. 2018a; Izotov et al. 2019; Izotov, Thuan & Guseva 2021).

Overall, we have observed three galaxies at $z \sim 8$ showing a large scatter in metallicity, probably as a consequence of their early evolutionary stage, questioning whether the FMR scaling relation observed at lower redshifts, and associated with a more smooth and secular evolution, is already in place at these cosmic epochs. However, much larger and statistically robust samples are required in order to draw any strong conclusion on the evolution of such scaling relation at these redshifts.

4.3 Comparison with theoretical predictions

Finally, in Fig. 6 we also compare our observations with the predictions of the MZR at $z \sim 8$ extracted from different suites of cosmological box and zoom-in simulations, namely IllustrisTNG (Marinacci et al. 2018; Naiman et al. 2018; Nelson et al. 2018, 2019; Pillepich et al. 2018; Springel et al. 2018), EAGLE (Crain et al. 2015; Schaye et al. 2015; McAlpine et al. 2016), FIRE (Ma et al. 2016), and SERRA (Pallottini et al. 2022). In both EAGLE and IllustrisTNG we make use of the publicly available subhalo catalogues at $z = 8$ from the highest resolution runs in $\sim 100^3$ cMpc³ cosmological boxes with fiducial subgrid physics prescriptions. In order to calculate gas phase metallicities in IllustrisTNG and EAGLE, we adopt the approach of Torrey et al. (2019), considering central galaxies and assuming that oxygen comprises 35 per cent of the SFR-weighted metal mass fraction within twice the stellar half-mass radius (IllustrisTNG) and 35 per cent of the metal mass fraction in star-forming gas particles in a bound halo (EAGLE). FIRE simulations instead define the gas-phase metallicity as the mass-weighted metallicity of all gas particles that belong to the ISM (defined by a temperature below 10^4 K, Ma et al. 2016), whereas in SERRA the metallicity is tracked as the sum of all heavy elements and gas, and stellar metallicity are coupled (Pallottini et al. 2022). Both FIRE and SERRA assume solar abundance ratios (Asplund et al. 2009).

In Fig. 6 we find that both EAGLE and IllustrisTNG are in reasonably good agreement with the observations of the two $z \sim 7.6$ galaxies with T_e measurements. In order to contextualize this result on the absolute metallicity scale, we have verified that our physical assumptions on oxygen yield provides good matches to both the parametrization of the MZR of Curti et al. (2020a) at $z \sim 0.08$ and of Sanders et al. (2021) at $z = 2-3$, which are based on T_e -calibrated strong-line diagnostics. This comparison hence suggests that both suites may capture some of the primary chemical enrichment in place in the early Universe, despite the lack of observational data available for model calibration at high redshift.

The redshift-evolution of the MZR predicted by FIRE simulations (Ma et al. 2016) (originally tracing galaxies from $z = 0-6$ and here extrapolated to $z \sim 8$) shows instead a much lower normalization, suggesting a strong evolution between $z \sim 3.3$ and $z \sim 8$, and getting closer to what we observe in ID4590. However, in contrast to what is found for EAGLE and IllustrisTNG, we find that the FIRE-based MZR parametrization from Ma et al. (2016) predicts 0.22 dex and 0.24 dex lower metallicities than observed in MOSDEF galaxies at $z \sim 2.3$ and $z \sim 3.3$ from Sanders et al. (2021), respectively, whereas 0.15 dex higher normalization compared to the SDSS-MZR at $z \sim 0.08$ from Curti et al. (2020a). We attempt to correct for such redshift-dependent offset by fitting an exponential function of the form $[A e^{-z/z_0} + C]$ ¹⁴ to the measured $\Delta \log(\text{O}/\text{H})$ in FIRE simulations at the three redshifts ($z \sim 0.08$, $z \sim 2.3$, $z \sim 3.3$), and use it to predict a normalization offset at $z \sim 8$ of $\Delta \log(\text{O}/\text{H}) = -0.25$ dex. In Fig. 6, we also show such re-scaled $z \sim 8$ extrapolation of the FIRE-MZR as the light-brown dashed line, which gets closer to what observed in ID10612. In contrast, the high-resolution (25 pc at $z = 8$) SERRA suite of cosmological zoom-in simulations predict a flatter MZR at $z \sim 8$ with much larger dispersion, suggesting such a scaling relation is not yet in place at these cosmic epochs. We note that the SERRA simulations follow galaxies only down to $z \sim 6$, hence no direct comparison with lower redshift observations can be performed. Needless to say, more metallicity determinations at such early epochs and more dedicated simulations of high-redshift galaxy populations are needed to constrain the theoretical predictions on the evolution of the MZR at very high- z relative to its shape at lower redshift.

5 CONCLUSIONS

We have analysed the properties of the three $z \sim 8$ gravitationally lensed galaxies observed in the framework of the *JWST* Early Release Observations. These galaxies were selected solely on their redshift $z > 7$. We have used sensitive NIRSspec spectra probing the rest-frame optical emission in these sources. Through a careful processing and inspection of the spectra, we could study the ISM properties in these galaxies, and apply the robust T_e -method to infer the gas-phase oxygen abundance for the first time at such high redshift. Our main findings for these three galaxies at $z \sim 8$ are summarized as follows:

- (i) The Balmer lines are consistent with some, low level of dust extinction (Fig. 2). This finding is also consistent with the analysis of the continuum SED.
- (ii) The excitation diagnostic ratios, such as $[\text{O III}]/\text{H}\beta$, $[\text{O II}]/\text{H}\beta$, and $[\text{O III}]/[\text{O II}]$ are in the tail of the distribution observed in galaxies at $z \sim 2-3$ (Fig. 3). Remarkably, some of them have very low $[\text{O II}]/\text{H}\beta$ and very high $[\text{O III}]/[\text{O II}]$. These are consistent with the

expectation of photoionization models for metal-poor galaxies and/or galaxies with high escape fraction of ionizing, Lyman continuum photons.

- (iii) We robustly detect the $[\text{O III}]\lambda 4363$ auroral line in all three galaxies, with ratios relative to the strong $[\text{O III}]\lambda\lambda 4959, 5007$ doublet that are large relative to local galaxies (0.01–0.04).

- (iv) The inferred gas temperatures range from $1.2 \cdot 10^4$ K to $2.8 \cdot 10^4$ K, with the T_e -based metallicities ranging from extremely metal poor ($12 + \log(\text{O}/\text{H}) \sim 7$) to about one third solar.

- (v) None of the local strong-line metallicity calibrations seem to provide a good prediction of the observed metallicities at $z \sim 8$ simultaneously across all diagnostics and for all galaxies (Fig. 5). Different calibrations seem to perform better for some galaxies or for some diagnostic ratios, suggesting that a systemic re-calibration of the strong-line diagnostics is needed for these early epochs.

- (vi) The two most ‘massive’ galaxies of the sample at $z \sim 7.6$ ($\log(M_*/M_\odot) = 8.1-8.7$) are scattered around the mass–metallicity relation at $z \sim 2-3$ (Fig. 6), potentially suggestive of little evolution of the MZR from $z \sim 2-3$ to $z \sim 8$. On the contrary, the least massive and most metal-poor galaxy ($\log(M_*/M_\odot) = 7.7$, $12 + \log(\text{O}/\text{H}) = 6.99$) deviates significantly from the relation at lower redshifts, suggesting that this galaxy is in a phase of rapid evolution or that the MZR has a much steeper slope at such low masses. Different cosmological simulations can reproduce some of the galaxies on the MZR, but none of them seem capable of simultaneously matching all of them.

- (vii) The three galaxies are widely scattered relative to the FMR, with two of them marginally consistent and one (ID4590 at $z \sim 8.5$) strongly deviating (Fig. 7). This finding suggest that galaxies at such early epochs are undergoing rapidly evolving mechanisms, and not yet settled on the local scaling relations that are instead associated with smooth, secular evolutionary processes. In any case, much larger samples are required in order to draw strong conclusions on the evolution of such scaling relations.

In conclusion, these first data sets already highlight the giant leap in the redshift parameter space brought to the field by the advent of rest-frame optical spectroscopy enabled by *JWST*, which is about to open a window on new modes of galaxy formation and evolution, helping us to discover objects with properties radically different than all the other known galaxies. Several forthcoming observational programmes will target the ‘redshift desert’ between $z \sim 3-8$ (and beyond), allowing us to obtain a complete and coherent picture of the evolution of the chemical properties of galaxies across the entire cosmic history.

None the less, we also stress that assessing the applicability of the strong-line metallicity diagnostics at high redshift remains an open problem, which requires both more a carefully selected sample of galaxies and deeper observations to detect auroral lines over a wider range of metallicities. While the observations discussed in this paper provide a preview of the possibilities opened by *JWST* in this sense, a variety of programmes scheduled in Cycle 1 primarily designed to address this science topic (e.g. Curti et al. 2021; Shapley et al. 2021; Strom et al. 2021) will soon provide a more robust re-calibration of the strong-line metallicity diagnostics for the high-redshift Universe.

ACKNOWLEDGEMENTS

We thank the anonymous referee for his/her comments which contributed to improving this paper.

We are also very grateful to the ERO and other teams who made these *JWST* observations possible. The Early Release Observations and associated materials were developed, executed, and compiled by

¹⁴best-fitting parameters: $A = 0.43$; $z_0 = 0.85$; $C = -0.25$

the ERO production team: Hannah Braun, Claire Blome, Matthew Brown, Margaret Caruthers, Dan Coe, Joseph DePasquale, Nestor Espinoza, Macarena Garcia Marin, Karl Gordon, Alaina Henry, Leah Hustak, Andi James, Ann Jenkins, Anton Koekemoer, Stephanie LaMassa, David Law, Alexandra Lockwood, Amaya Moro-Martín, Susan Mullally, Alyssa Pagan, Dani Player, Klaus Pontoppidan, Charles Proffitt, Christine Pulliam, Leah Ramsay, Swara Ravindranath, Neill Reid, Massimo Robberto, Elena Sabbi, Leonardo Ubeda. The EROs were also made possible by the foundational efforts and support from the JWST instruments, STScI planning and scheduling, and Data Management teams.

MC, RM, FD'E, LS, JS, WB, JW, TJL, CH-P, and JSB acknowledge support by the Science and Technology Facilities Council (STFC) and ERC Advanced Grant 695671 'QUENCH'. RM also acknowledges funding from a research professorship from the Royal Society. SC acknowledges support from the ERC Advanced Grant INTERSTELLAR H2020/740120. HÜ gratefully acknowledges support by the Isaac Newton Trust and by the Kavli Foundation through a Newton-Kavli Junior Fellowship. SA acknowledges funding from grant PID2021-127718NB-I00 by the Spanish Ministry of Science and Innovation/State Agency of Research (MCIN/AEI). JMP and JW gratefully acknowledge support from the MERAC Foundation. AJB acknowledges funding from the 'FirstGalaxies' Advanced Grant from the European Research Council (ERC) under the European Union's Horizon 2020 research and innovation programme (Grant agreement No. 789056). RS acknowledges support from an STFC Ernest Rutherford Fellowship (ST/S004831/1). ECL acknowledges support of an STFC Webb Fellowship (ST/W001438/1). We are grateful to Pierre Ferruit, Peter Jakobsen, and Nora Lützgendorf for sharing their expertise on NIRSpec and the processing of its unique data.

This work is based on observations made with the NASA/ESA/CSA *James Webb Space Telescope*. Some of the data presented in this paper were obtained from the Multimission Archive at the Space Telescope Science Institute (MAST). STScI is operated by the Association of Universities for Research in Astronomy, Inc., under NASA contract NAS5-26555. Support for MAST for non-*HST* data is provided by the NASA Office of Space Science via grant NAG5-7584 and by other grants and contracts.

Finally, MC is heartily grateful to Vittoria for showing him a completely new and wonderful, yet unknown and mysterious, part of the Universe.

DATA AVAILABILITY

The raw (level 2) data underlying this article are publicly available from the MAST archive. The processed and calibrated ID spectra analysed in this work are publicly available at <https://doi.org/10.5281/zenodo.6940561>. Other data are available upon reasonable request to the corresponding author.

REFERENCES

- Allende Prieto C., Lambert D. L., Asplund M., 2001, *ApJ*, 556, L63
 Andrews B. H., Martini P., 2013, *ApJ*, 765, 140
 Arellano-Córdova K. Z., 2022, preprint (arXiv:2208.02562)
 Asplund M., Grevesse N., Sauval A. J., Scott P., 2009, *ARA&A*, 47, 481
 Baldwin J. A., Phillips M. M., Terlevich R., 1981, *PASP*, 93, 5
 Barrow K. S. S., Robertson B. E., Ellis R. S., Nakajima K., Saxena A., Stark D. P., Tang M., 2020, *ApJ*, 902, L39
 Berg D. A. et al., 2012, *ApJ*, 754, 98
 Bian F., Kewley L. J., Dopita M. A., 2018, *ApJ*, 859, 175
 Bohlin R. C., Gordon K. D., Tremblay P. E., 2014, *PASP*, 126, 711
 Bohlin R. C., Hubeny I., Rauch T., 2020, *AJ*, 160, 21
 Bouché N. et al., 2010, *ApJ*, 718, 1001
 Brinchmann J., Charlot S., White S. D. M., Tremonti C., Kauffmann G., Heckman T., Brinkmann J., 2004, *MNRAS*, 351, 1151
 Brinchmann J., 2022, preprint (arXiv:2208.07467)
 Caminha G. B., Suyu S. H., Mercurio A., Brammer G., Bergamini P., Vanzella E., Acebron A., 2022, preprint (arXiv:2207.07567)
 Cappellari M., 2017, *MNRAS*, 466, 798
 Carnall A. C. et al., 2022, preprint (arXiv:2207.08778)
 Carnall A. C., McLure R. J., Dunlop J. S., Davé R., 2018, *MNRAS*, 480, 4379
 Chabrier G., 2003, *PASP*, 115, 763
 Chevillard J., Charlot S., 2016, *MNRAS*, 462, 1415
 Chisholm J. et al., 2022, preprint (arXiv:2207.05771)
 Choi J., Dotter A., Conroy C., Cantiello M., Paxton B. D., 2016, *ApJ*, 823, 102
 Christensen L. et al., 2012, *MNRAS*, 427, 1973
 Conroy C., Naidu R. P., Zaritsky D., Bonaca A., Cargile P., Johnson B. D., Caldwell N., 2019, *ApJ*, 887, 237
 Crain R. A. et al., 2015, *MNRAS*, 450, 1937
 Cresci G., Mannucci F., Curti M., 2019, *A&A*, 627, A42
 Cresci G., Mannucci F., Sommariva V., Maiolino R., Marconi A., Brusa M., 2012, *MNRAS*, 421, 262
 Curti M. et al., 2020b, *MNRAS*, 492, 821
 Curti M. et al., 2021, Opening the era of direct metallicity measurements in high redshift galaxies, JWST Proposal. Cycle 1, ID. #1879
 Curti M. et al., 2022, *MNRAS*, 512, 4136
 Curti M., Cresci G., Mannucci F., Marconi A., Maiolino R., Esposito S., 2017, *MNRAS*, 465, 1384
 Curti M., Mannucci F., Cresci G., Maiolino R., 2020a, *MNRAS*, 491, 944
 Davé R., Rafieeferantsoa M. H., Thompson R. J., Hopkins P. F., 2017, *MNRAS*, 467, 115
 Díaz A. I., Castellanos M., Terlevich E., Luisa García-Vargas M., 2000, *MNRAS*, 318, 462
 Dors O. L., Contini M., Riffel R. A., Pérez-Montero E., Krabbe A. C., Cardaci M. V., Hägele G. F., 2021, *MNRAS*, 501, 1370
 Ebeling H. et al., 2013, *MNRAS*, 432, 62
 Ebeling H., Barrett E., Donovan D., Ma C. J., Edge A. C., van Speybroeck L., 2007, *ApJ*, 661, L33
 Ebeling H., Edge A. C., Henry J. P., 2001, *ApJ*, 553, 668
 Ebeling H., Edge A. C., Mantz A., Barrett E., Henry J. P., Ma C. J., van Speybroeck L., 2010, *MNRAS*, 407, 83
 Ellison S. L., Patton D. R., Simard L., McConnachie A. W., 2008, *ApJ*, 672, L107
 Erb D. K., Pettini M., Steidel C. C., Strom A. L., Rudie G. C., Trainor R. F., Shapley A. E., Reddy N. A., 2016, *ApJ*, 830, 52
 Ferruit P. et al., 2022, *A&A*, 661, A81
 Garnett D. R., 1990, *ApJ*, 363, 142
 Gordon K. D. et al., 2022, *AJ*, 163, 267
 Gordon K. D., Clayton G. C., Misselt K. A., Landolt A. U., Wolff M. J., 2003, *ApJ*, 594, 279
 Hayden-Pawson C. et al., 2022, *MNRAS*, 512, 2867
 Izotov Y. I., Guseva N. G., Fricke K. J., Henkel C., 2019, *A&A*, 623, A40
 Izotov Y. I., Thuan T. X., Guseva N. G., 2017, *MNRAS*, 471, 548
 Izotov Y. I., Thuan T. X., Guseva N. G., 2021, *MNRAS*, 504, 3996
 Izotov Y. I., Thuan T. X., Guseva N. G., Liss S. E., 2018a, *MNRAS*, 473, 1956
 Izotov Y. I., Worseck G., Schaerer D., Guseva N. G., Thuan T. X., Fricke Verhamme A., Orlitová I., 2018b, *MNRAS*, 478, 4851
 Jakobsen P. et al., 2022, *A&A*, 661, A80
 Johnson B. D., Leja J., Conroy C., Speagle J. S., 2021, *ApJS*, 254, 22
 Katz H., 2022 *MNRAS*, in press 2022 MNRAS.tmp.2470
 Kewley L. J., Nicholls D. C., Sutherland R. S., 2019, *ARA&A*, 57, 511
 Kojima T. et al., 2020, *ApJ*, 898, 142
 Lamareille F., 2010, *A&A*, 509, A53

- Langan I., Ceverino D., Finlator K., 2020, *MNRAS*, 494, 1988
- Lilly S. J., Carollo C. M., Pipino A., Renzini A., Peng Y., 2013, *ApJ*, 772, 119
- Luridiana V., Morisset C., Shaw R. A., 2012, in Manchado A., Stanghellini L., Schönberner D., eds, Proc. IAU Symp. 283, Planetary Nebulae: An Eye to the Future. Cambridge Univ. Press, Cambridge, p. 422
- Luridiana V., Morisset C., Shaw R. A., 2015, *A&A*, 573, A42
- Ma X., Hopkins P. F., Faucher-Giguère C.-A., Zolman N., Muratov A. L., Kereš D., Quataert E., 2016, *MNRAS*, 456, 2140
- Madau P., Dickinson M., 2014, *ARA&A*, 52, 415
- Mahler G. et al., 2022, preprint (arXiv:2207.07101)
- Maiolino R. et al., 2008, *A&A*, 488, 463
- Maiolino R., Mannucci F., 2019, *A&AR*, 27, 3
- Mann A. W., Ebeling H., 2012, *MNRAS*, 420, 2120
- Mannucci F. et al., 2009, *MNRAS*, 398, 1915
- Mannucci F., Cresci G., Maiolino R., Marconi A., Gnerucci A., 2010, *MNRAS*, 408, 2115
- Mannucci F., Salvaterra R., Campisi M. A., 2011, *MNRAS*, 414, 1263
- Marinacci F. et al., 2018, *MNRAS*, 480, 5113
- Marino R. A. et al., 2013, *A&A*, 559, A114
- McAlpine S. et al., 2016, *Astron. Comput.*, 15, 72
- Nagao T., Maiolino R., Marconi A., 2006, *A&A*, 459, 85
- Nagao T., Murayama T., Taniguchi Y., 2001, *ApJ*, 549, 155
- Naiman J. P. et al., 2018, *MNRAS*, 477, 1206
- Nakajima K. et al., 2022, *ApJS*, 262, 3
- Nakajima K., Ellis R. S., Robertson B. E., Tang M., Stark D. P., 2020, *ApJ*, 889, 161
- Nakajima K., Maiolino R., 2022, *MNRAS*, 513, 5134
- Nakajima K., Ouchi M., 2014, *MNRAS*, 442, 900
- Nelson D. et al., 2018, *MNRAS*, 475, 624
- Nelson D. et al., 2019, *Comput. Astrophys. Cosmol.*, 6, 2
- Nicholls D. C., Dopita M. A., Sutherland R. S., Kewley L. J., Palay E., 2013, *ApJS*, 207, 21
- Noeske K. G. et al., 2007, *ApJ*, 660, L47
- Onodera M. et al., 2016, *ApJ*, 822, 42
- Osterbrock D. E., Ferland G. J., 2006, *Astrophysics of Gaseous Nebulae and Active Galactic Nuclei*, 2nd edn.. University Science Books, Sausalito, CA
- Palay E., Nahar S. N., Pradhan A. K., Eissner W., 2012, *MNRAS*, 423, L35
- Pallottini A. et al., 2022, *MNRAS*, 513, 5621
- Pascale M. et al., 2022, preprint (arXiv:2207.07102)
- Patrício V., Christensen L., Rhodin H., Cañameras R., Lara-López M. A., 2018, *MNRAS*, 481, 3520
- Perrin M. D., Long J., Sivaramakrishnan A., Lajoie C.-P., Elliot E., Pueyo L., Albert L., 2015, *WebbPSF: James Webb Space Telescope PSF Simulation Tool*, Astrophysics Source Code Library, record ascl:1504.007
- Pettini M., Pagel B. E. J., 2004, *MNRAS*, 348, L59
- Pillepich A. et al., 2018, *MNRAS*, 475, 648
- Pilyugin L. S., Grebel E. K., 2016, *MNRAS*, 457, 3678
- Pilyugin L. S., Mattsson L., Vílchez J. M., Cedrés B., 2009, *MNRAS*, 398, 485
- Pontoppidan K. M. et al., 2022, *ApJ*, 936, L14
- Popesso P. et al., 2022, preprint (arXiv:2203.10487)
- Repp A., Ebeling H., 2018, *MNRAS*, 479, 844
- Repp A., Ebeling H., Richard J., 2016, *MNRAS*, 457, 1399
- Rhoads J. E., 2022, preprint (arXiv:2207.13020)
- Riffel R. A. et al., 2021, *MNRAS*, 501, L54
- Sanders R. L. et al., 2016, *ApJ*, 816, 23
- Sanders R. L. et al., 2020, *MNRAS*, 491, 1427
- Sanders R. L. et al., 2021, *ApJ*, 914, 19
- Sandles L., Curtis-Lake E., Charlot S., Chevallard J., Maiolino R., 2022, *MNRAS*, 515, 2951
- Schaerer D., Marques-Chaves R., Barrufet L., Oesch P., Izotov Y.I., Naidu R., Guseva N. G., Brammer G., 2022, *A&A*, 665, 6
- Schaye J. et al., 2015, *MNRAS*, 446, 521
- Schneider R., Hunt L., Valiante R., 2016, *MNRAS*, 457, 1842
- Shapley A. E. et al., 2015, *ApJ*, 801, 88
- Shapley A. E. et al., 2017, *ApJ*, 846, L30
- Shapley A. E. et al., 2021, The AURORA Survey: First Direct Metallicity Calibrations at High Redshift, JWST Proposal. Cycle 1, ID. #1914
- Shivaei I. et al., 2020, *ApJ*, 899, 117
- Springel V. et al., 2018, *MNRAS*, 475, 676
- Stasinska G., 2002, in Esteban C., López R. J. G., Herrero A., Sánchez F., eds, *Cosmochemistry. The Melting Pot of the Elements*. Cambridge Univ. Press, Cambridge, p. 115
- Steidel C. C. et al., 2014, *ApJ*, 795, 165
- Strom A. L., Rudie G. C., Chen Y., Law D. R., Maseda M., Steidel C. C., Trainor R. F., 2021, CECILIA: A direct-method metallicity calibration for Cosmic Noon through the Epoch of Reionization, JWST Proposal. Cycle 1, ID. #2593
- Strom A. L., Steidel C. C., Rudie G. C., Trainor R. F., Pettini M., 2018, *ApJ*, 868, 117
- Strom A. L., Steidel C. C., Rudie G. C., Trainor R. F., Pettini M., Reddy N. A., 2017, *ApJ*, 836, 164
- Tacchella S. et al., 2022, *ApJ*, 927, 170
- Tang M., Stark D. P., Chevallard J., Charlot S., 2019, *MNRAS*, 489, 2572
- Taylor A. J., 2022, preprint (arXiv:2208.06418)
- Topping M. W., Shapley A. E., Reddy N. A., Sanders R. L., Coil A. L., Kriek M., Mobasher B., Siana B., 2020, *MNRAS*, 495, 4430
- Torrey P. et al., 2019, *MNRAS*, 484, 5587
- Tremonti C. A. et al., 2004, *ApJ*, 613, 898
- Troncoso P. et al., 2014, *A&A*, 563, A58
- Trump J. R., 2022, preprint (arXiv:2207.12388)
- Witstok J., Smit R., Maiolino R., Curti M., Laporte N., Massey R., Richard J., Swinbank M., 2021, *MNRAS*, 508, 1686
- Zahid H. J., Dima G. I., Kudritzki R.-P., Kewley L. J., Geller M. J., Hwang H. S., Silverman J. D., Kashino D., 2014, *ApJ*, 791, 130
- Zahid H. J., Kewley L. J., Bresolin F., 2011, *ApJ*, 730, 137

¹Kavli Institute for Cosmology, University of Cambridge, Madingley Road, Cambridge CB3 0HA, UK

²Cavendish Laboratory – Astrophysics Group, University of Cambridge, 19 JJ Thompson Avenue, Cambridge CB3 0HE, UK

³Scuola Normale Superiore, Università di Pisa, Piazza dei Cavalieri 7, I-56126 Pisa, Italy

⁴Department of Physics and Astronomy, University College London, Gower Street, London WC1E 6BT, UK

⁵Institute of Astronomy, University of Cambridge, Madingley Road, Cambridge CB3 0HA, UK

⁶Sorbonne Université, UPMC-CNRS, UMR7095, Institut d’Astrophysique de Paris, F-75014 Paris, France

⁷National Astronomical Observatory of Japan, 2-21-1 Osawa, Mitaka, Tokyo 181-8588, Japan

⁸INAF – Osservatorio Astrofisico di Arcetri, Largo E. Fermi 5, I-50125 Florence, Italy

⁹Dipartimento di Fisica e Astronomia, Università di Firenze, Via G. Sansone 1, I-50125 Sesto Fiorentino (Florence), Italy

¹⁰Centro de Astrobiología (CAB), CSIC-INTA, Cra. de Ajalvir Km. 4, Torrejón de Ardoz, E-28850 Madrid, Spain

¹¹Cosmic Dawn Center, Niels Bohr Institute, University of Copenhagen, Rådmandsgade 62, DK-2200 Copenhagen N, Denmark

¹²Department of Physics, University of Oxford, Denys Wilkinson Building, Keble Road, Oxford OX1 3RH, UK

¹³Centre for Astrophysics Research, Department of Physics, Astronomy and Mathematics, University of Hertfordshire, Hatfield AL10 9AB, UK

¹⁴AURA for the European Space Agency, Space Telescope Science Institute, 3700 San Martin Drive, Baltimore, MD 21218, USA

¹⁵Department of Astronomy, University of Wisconsin-Madison, 475 N. Charter St., Madison, WI 53706, USA

¹⁶Astrophysics Research Institute, Liverpool John Moores University, 146 Brownlow Hill, Liverpool L3 5RF, UK